SCIENTIFIC REPORTS

OPEN

# A composite of platelet-like orientated $BiVO_4$ fused with MIL-125(Ti): Synthesis and characterization

Received: 28 January 2019
Accepted: 1 July 2019
Published online: 11 July 2019

Philani Vusumuzi Hlophe, Lwazi Charles Mahlalela & Langelihle Nsikayezwe Dlamini

**The development of heterojunctions is the current focus of the scientific community as these materials are visible light active and the staggered positioning of their band edges combats electron-hole recombination which is the downside of most photocatalysts. In this work, a two- step hydrothermal synthesis protocol was utilized to fabricate a novel observable-light active material, composed of platelet-like $BiVO_4$ and a titanium-based metal organic framework (MOF) called MIL-125(Ti). The tuning of specific morphologies, such as platelet-like in $BiVO_4$, provides the exposure of most reactive facets which are more reactive towards photooxidation of organics in water, thus increasing their efficiency. The as-synthesized heterojunction was characterized by Transmission electron microscopy (TEM), scanning transmission microscopy (SEM), X-Ray diffraction (XRD), Raman spectroscopy, ultraviolet-visible diffuse reflectance spectra (UV-Vis DRS), X-Ray photoelectron spectroscopy (XPS) and photoluminescence (PL) spectra. The formation of the heterojunction lead to a positive shift of the 3-2 Bi:Ti valence band (VB) (1.78 eV) when compared to 1.27 eV VB position of $BiVO_4$. The PL and photoelectrochemical measurements revealed that the heterojunction photocatalyst designated 3-2 Bi-Ti demonstrated inhibited recombination rate (platelet-like $BiVO_4$ > 3-2 Bi:Ti (PM) > MIL-125 > 1–1 Bi:Ti > 2–3 Bi:Ti > 3-2 Bi:Ti) and highly efficient interfacial charge shuttle between platelet-like $BiVO_4$ and MIL-125(Ti) through the formed *n-n* junction.**

Several photocatalyst uses have been reported in literature and they include uses such as for storage of energy, sterilization, self-cleaning, air purification and wastewater treatment[1,2]. Work in these areas have been vastly explored using $TiO_2$ as the base photocatalyst[3]. The application of $TiO_2$ is only limited to UV absorption, due to its large band gap, which leads to low efficiency for the visible spectrum and high recombination rate[4].

Even though there are available visible light active photocatalysts that have been used in photodegradation, such as $BiVO_4$ and $WO_3$, they further face an issue with fast electron-hole pairs recombination[5,6]. This fast recombination of the electron-hole pairs allows only for few electrons and holes to migrate to the surface and participate in catalytic reactions on the surface of the photocatalyst which results in poor efficiency thus stagnating industrial application[7].

The synthesis of composite materials with the aim to formulate a heterojunction has been explored as one of the important strategies for the separation of electron-hole pairs in photocatalytic semiconductor materials. Heterojunction formation is a spatial separation technique which is band-edge offset dependant. These band-edge offsets separate electrons and holes by directing these charge carriers to different materials via a junction[8]. This allows the electrons and holes to spend more time apart, enough for reduction and oxidation to occur[7].

Considerable attention has been given to bismuth vanadate ($BiVO_4$) due to its narrow band gap of 2.4–2.5 eV, low-cost, nontoxicity, and favourable valence band position. These characteristics have enabled $BiVO_4$ to emerge as a promising candidate for photoelectrochemical (PEC) water splitting and photocatalytic degradation of organic pollutants[9]. $BiVO_4$ is intrinsically an *n*-type semiconductor that has a valance band position that is appropriate for visible-light activity[10]. Crystal polymorphs of $BiVO_4$ include; zircon structure with a tetragonal system (z-t), scheelite structures with monoclinic (s-m) and tetragonal (s-t) phases[11]. Among these three phases,

Department of Chemical Sciences, University of Johannesburg, Doornfontein Campus, P.O. Box 17011, Doornfontein, Johannesburg, 2028, South Africa. Correspondence and requests for materials should be addressed to L.N.D. (email: lndlamini@uj.ac.za)

the monoclinic phase has been reported to be thermodynamically stable and demonstrates good photoactivity properties[9].

Even though $BiVO_4$ has shown good visible light activity, it suffers from slow electron transportation which is linked to fast recombination of photogenerated electron-hole pairs. Many attempts have been made to combat this through co-catalyst modifications to form heterojunctions or phase-junctions, doping with non-metals or metals such as Fe, W, N, P and Mo, and tuning morphology with the aim to expose most reactive facets[10]. Doping involves the introduction of impurity levels that act as electron or hole traps thus facilitation separation of electrons and holes[12,13]. Co-catalyst modifications to form heterojunctions or phase-junctions depends on the band-edge staggered alignment that facilitate the shuttle of electrons and holes to different materials by separating the respective charge transporters. This has been made possible by using $FeVO_4$, $Bi_2O_3$ and $TiO_2$ to form heterostructures with $BiVO_4$[14–16]. While phase junctions have been synthesized through the formation of monoclinic and tetragonal phases co-existing in one $BiVO_4$ sample for spatial separation of electron-hole pairs through band-edge offsets resulting from the differences band positions of the different phases[17].

$BiVO_4$ is known to suffer from low surface area, thus in this work platelet-like $BiVO_4$ was synthesized in hyperbranched polyethyleneimine (HPEI) to improve surface area and produce smaller nanoparticles. Facet design in $BiVO_4$ has shown that the 010 facet is the most reactive and provides spatial separation of electrons and holes by increasing the availability of electrons on its surface while preventing electron hole recombination[18]. Tan *et al*. illustrated higher photooxidation activity of {010} facet of monoclinic $BiVO_4$ in relative exposure extents with {110} facet, where the {110} traps holes while the electrons are trapped by the largely exposed {010} facet[18]. Huang *et al*. reported a correlated high activity to {010} facets of $BiVO_4$ for the evolution of $O_2$[19]. The novelty of this work is the tuning of the most reactive facet of $BiVO_4$ whilst also using HPEI as a template for the development stable nanoparticles.

Hyperbranched polyethyleneimine belongs to a class of materials identified as dendrimers as it a branched macromolecule which consists of a diaminoethane core, interior branching polyethyleneimine intermediates and an abundance of surrounding $NH_2$ functional groups which make the molecule hydrophilic[20,21]. The interior branching units render multiple internal nanocavities which can be utilized as a host for the production of small and robust nanoparticles because HPEI has a quasi-spherical structure that provides a shell which inhibits the aggregation of nanoparticles[21].

Metal–Organic Frameworks (MOFs) are a category of translucent substances that comprise of coordinate bonds between metal nodes and organic ligands[22]. MOFs have come to the fore as a comprehensive set of crystalline materials with well-defined porosity. MOFs are different from other permeable materials, they boast many merits such as well-defined porosity, large surface area, ease of synthesis, thermal stability, ultra-low densities and with extensive properties convenient for physical and chemical implementation[23]. These intriguing features have triumphed the implementation of MOFs in gas storage, catalysis, segregation of fluids[24]. However, the limitation of these materials is the lack of visible light activation, which limits their efficiency upon photon irradiation.

Recently research focus has been on the photoactive, crystalline and highly porous titanium oriented MOFs including MIL-125(Ti) exhibiting $Ti_8O_8(OH)_4(BDC)_6$ BDC = 1,4-benzenedicarboxylic acid has garnered tremendous recognition in the photocatalysis domain[25].

MIL-125(Ti) is a crystal clear titanium dicarboxylate exhibiting outstanding absorbance ability, encapsulation potential and good permeability, thermal strength and interesting photochemical characteristics[22]. As a result of the frameworks porosity, the secondary building units (SBUs) transport reductive intermediates away from the reactive sites. This is because the material has a rigid coordination environment ideal to create chromophore sites by introducing metal co-catalysts to the SBUs. Additionally this material is decorated with numerous inactive Ti sites[22]. However, its application in photocatalytic platforms is limited due to its activation only in the UV light region and fast charge recombination, resulting in poor photocatalytic efficiency. Not much work has been reported on fusing MIL-125(Ti) and facet controlled $BiVO_4$ composite, with the potential of being used in various photocatalytic applications such as environmental remediation. Thus, in this work we report the combination of platelet-like $BiVO_4$ with MIL-125(Ti) into a novel heterojunction photocatalyst which will enable the material to have minimum recombination and be photoactive in visible light.

## Materials and Methods

**Materials.** The chemicals were used as received from manufacturers and they included; bismuth nitrate pentahydrate (98% reagent grade, Sigma-Aldrich Co.), ammonium metavanadate (≥99% ACS reagent, Sigma-Aldrich Co.), nitric acid (55%, Associated Chemical Enterprises), ethanol (≥99.8% absolute, Sigma-Aldrich Co.), ammonia solution (25% Associated Chemical Enterprises), nitric acid (55%, Sigma-Aldrich Co.), hyperbranched polyethyleneimine (Sigma-Aldrich Co.), sodium sulphate (≥99% ReagentPlus, Sigma-Aldrich Co.), polyvinylidene fluoride (GPC, Sigma-Aldrich Co.), *N*-methylpyridine (≥99% ACS reagent, Sigma-Aldrich Co.), Teraphthalic acid (BDC) (Sigma-Aldrich Co.), *N*,*N*-dimethylformanide (DMF) (Sigma-Aldrich), titanium isopropoxide (Sigma-Aldrich Co.) and methanol (Sigma-Aldrich).

**Synthesis of nanoparticles.** Pristine MIL-125(Ti) was fabricated according to a synthesis route reported by Yang *et al*.[26] with minor adjustments. Typically, 2.2 g of teraphthalic acid was dissolved in a solution of 36 mL DMF and 4 mL methanol. Titanium isopropoxide (2.4 mL) was then added to the resultant solution which resulted in a white solution. This was then sonicated for 5 mins to ensure a homogeneous mixture. The mixture was exposed to hydrothermal conditions in a 100 mL Teflon lined autoclave for 24 hr at 150 °C. Post cooling to room temperature, a gel-like solid was secured which was washed once with 50 mL DMF and twice with 50 mL Methanol. The solid was then dried for 24 hrs at 60 °C in air.

Platelet-like $BiVO_4$ nanoparticles (NPs) were synthesized using a hydrothermal method with minor modifications as reported in one of our publications in the group[27]. Bismuth nitrate pentahydrate (4.90 g) and 1.20 g

ammonium metavanadate were dissolved in 60 mL of 2 M nitric acid and the solution was stirred for 2 hrs until a yellow precipitate. In this solution, 3.75 g HPEI was then added, after which the pH was adjusted to pH 2 using 25% ammonia solution. NaCl (1.75 g) was added and the solution was stirred for 15 min. The solution was then subjected to hydrothermal conditions in a 100 mL Teflon lined autoclave and heated in an oven at 200 °C for 24 hrs.

Three heterojunctions of $BiVO_4$/MIL-125(Ti) were synthesized via a coprecipitation method. The amounts in composites were based on Bi:Ti in the ratios 1:1, 2:3 and 3:2. The 3:2 composite was synthesized by measuring 0.972 g of platelet-like $BiVO_4$ which was mixed by sonication with 0.50 g teraphthalic acid, 0.6 mL titanium isopropoxide, 9.0 mL DMF and 1.0 mL methanol for 5 min. The mixture was then subjected to similar hydrothermal conditions as those of pristine MIL-125(Ti) stated above. For the other composites, 0.648 g platelet-like $BiVO_4$ was mixed with 0.80 g teraphthalic acid, 0.9 mL titanium isopropoxide, 13.3 mL DMF and 1.5 mL methanol for 2:3, while for 1:1, 0.324 g platelet-like $BiVO_4$ was mixed with 0.30 g teraphthalic acid, 0.3 mL titanium isopropoxide, 0.45 mL DMF and 0.5 mL methanol. These were subjected to similar conditions as those of the 3:2 composite synthesis method. The composites were named as 1–1 Bi:Ti, 2–3 Bi:Ti and 3-2 Bi:Ti.

A physically mixed (PM) sample of the 3:2 ratio of Bi:Ti was also synthesized for the purpose of electrochemical impedance spectroscopy (EIS) characterization to give an insight on the formation of Schottky contacts in the hydrothermally synthesized heterojunction compared to physical mixing. This was necessary to also give proof that their formation in the hydrothermally synthesized materials enable the separation of electrons and holes compared to a physically mixed sample. Platelet-like $BiVO_4$ (0.972 g) was mixed with 0.648 g of pristine MIL-125(Ti) using a pestle and mortar until a homogeneous mixture. This composite was named 3-2 Bi:Ti (PM).

**Characterization techniques.** Morphologies of the NPs were captured using scanning electron microscopy (SEM) and transmission electron microscopy (TEM). The SEM (TESCAN Vega TC) was operated at 20 kV operating voltage under nitrogen gas using VEGA 3 TESCAN software. Elemental composition of the NPs was elucidated with the SEM coupled with EDS and was operated at 20 kV. A TEM which was operated at an accelerating voltage of 200 kV was used to further acquire images of the NPs. The NPs were deposited on carbon coated copper grids after being dispersed in ethanol. Selected area electron diffraction (SAED) was conducted on the NPs at 20–25 k magnification to elucidate their crystal phases.

Powdered X-ray diffraction (X'Pert Philips) with CuK$\alpha$ radiation (0.1540 nm) polychomator beam in the 2$\theta$ scan range 20–80 °C was carried to confirm the crystal phases of the NPs from the SAED patterns. A step size and step time of 0.0170 (2$\theta$) and 87.63 s was used at 40 kV and 40 mA instrument power settings. Raman data were recorded for further confirmation of the crystal phases of the NPs. A Raman spectrometer, Raman Micro 200, Perkin Elmer precisely used with a single monochromator, a holographic notch and a cooled TCD. The samples were exposed for 4 s during excitation using the 514.5 nm $Ar^+$ line. Optical properties were recorded from a diffuse reflectance spectroscopy (DRS) on a Shimadzu UV-2450 UV-Vis spectrophotometer. $BaSO_4$ was used as a reference. Measurement of X-Ray photoelectron spectroscopy was carried out with a Thermo spectroscope, model ESCAlab 250Xi using a monochromator Al K$\alpha$ (1486.7 eV) as an excitation source at a working pressure of $<10^{-8}$ mBar. The photoluminescence spectra were recorded using a LS 45 fluorescence spectrometer (Perkin Elmer, precisely) at 242 nm wavelength.

Electrochemical measurements were conducted using Gamry IFC1000-11085 potentiostat in a standard three electrode system using Ag/AgCl as a reference electrode, a Pt wire as a counter electrode and a working electrode fabricated using fluorine-doped tin oxide (FTO) glass with NPs pasted on the fluorine-doped side. The working electrodes were prepared by mixing the synthesized NPs with polyvinylidene fluoride (PVDF) in a ratio 10:1 respectively in 1 mL N-methylpyridine (NMP). The PVDF was used as a binder and the NMP as a solvent to form a homogeneous slurry. The slurry was then drop casted on the FTO glass and allowed to dry overnight at room temperature. Electrical connection to the potentiostat was facilitated by attaching a copper wire using silver paste which was allowed to dry in air for 24 hr at room temperature. The electrochemical impedance spectroscopy (EIS) spectra was conducted at a frequency range of 10 kHz to 0.1 Hz at an AC voltage of 10 mV rms vs $E_{ref}$.

## Results and Discussion

The images in Fig. 1 show the morphologies of the synthesized pristine materials and subsequent composites. More precisely, Fig. 1a represents the SEM image of MIL-125(Ti) which are rectangular shaped blocks. The SEM-EDS mapping confirmed the MIL-125(Ti) materials comprised of titanium, oxygen and carbon elements (Figure S1). $BiVO_4$ NPs are shown in Fig. 1a which affirmed successful synthesis of platelet-like NPs. The SAED-EDS mapping in Figure S1b confirmed the presence of all the expected elements, mainly bismuth, vanadium and oxygen. Figure 1(c–e) represents the different composites fabricated which are 1–1, 2–3 and 3-2 Bi:Ti respectively. In all the composites the was an appearance of both the blocked and platelet-like NPs representing the presence of MIL-125(Ti) and $BiVO_4$ NPs respectively. This showed the successful formation of the heterojunction materials. Further justification of the fabrication of the aforementioned materials is presented in Figs S3–5 (SEM-EDS mapping) which showed the presence of bismuth, vanadium, titanium, carbon and oxygen.

Figure 2 illustrates the TEM images of the pristine MIL-125(Ti) and platelet-like $BiVO_4$ NPs. As evidenced by the SEM pictorial illustrations, the TEM confirmed the block and platelet-like NPs. The SAED patterns shown by Fig. 2c reveal the spots for platelet-like $BiVO_4$ and this confirmed the synthesis of monoclinic $BiVO_4$. The miller indices (042) and (002) shown are reported in literature to be those of monoclinic $BiVO_4$. Composite material's TEM images are depicted by Fig. 3(a–c) which confirmed the synthesis of the heterojunctions as the was an observation of both blocks and platelet-like NPs. In the 1–1 composite, the $BiVO_4$ is shown to be deposited on the MIL-125(Ti). While for 2–3 and 3-2 some on the MIL-125(Ti) blocks were slightly attached to the platelet-like NPs. For all the composite materials, the observed SAED patterns confirmed monoclinic $BiVO_4$ as the elucidated miller indices (042), (022), (011) in 1–1, 2–3 and 3-2 respectively are monoclinic spots. The were no record SAED

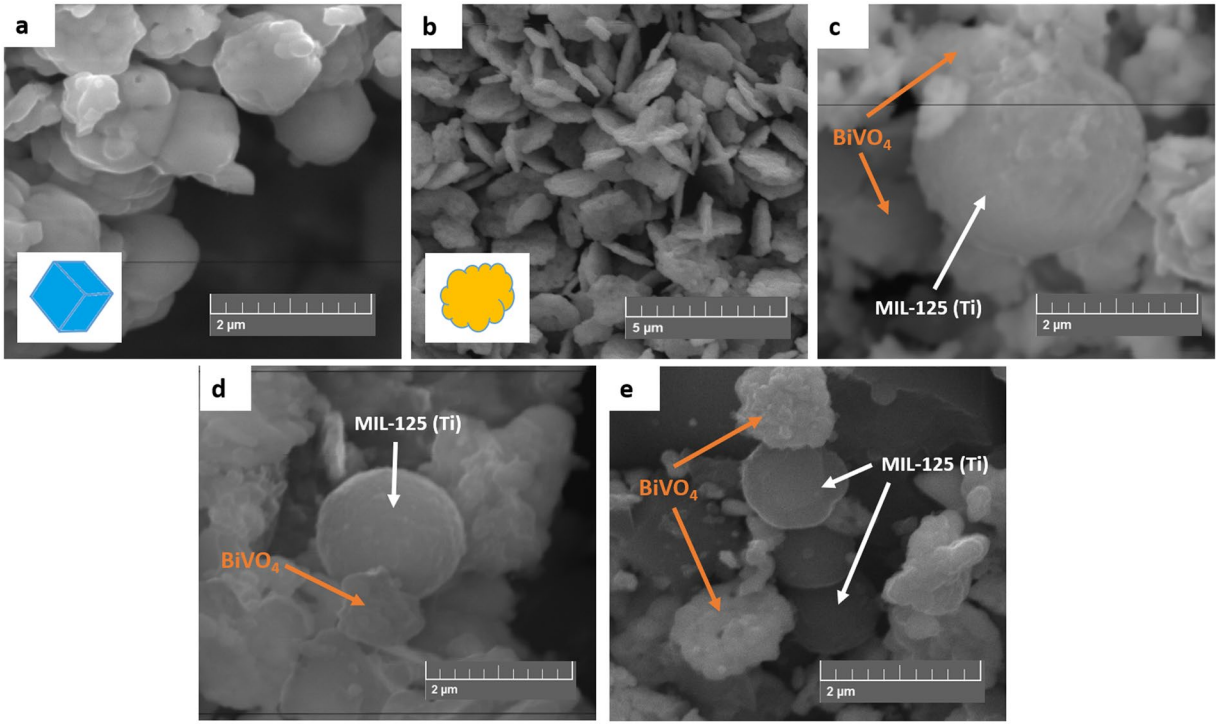


**Figure 1.** SEM images of (**a**) MIL-125(Ti), (**b**) $BiVO_4$, (**c**) 1–1 Bi:Ti, (**d**) 2–3 Bi:Ti and (**e**) 3-2 Bi:Ti. The inserts in (**a**) and (**b**) are redrawn morphologies of the pristine MIL-125(Ti) and platelet-like $BiVO_4$ respectively.

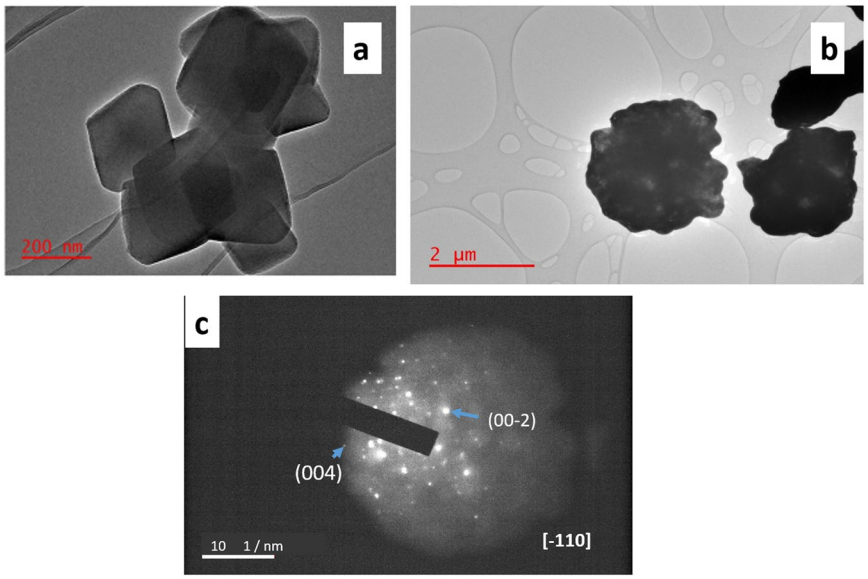


**Figure 2.** TEM images (**a**) MIL-125(Ti) (**b**) $BiVO_4$. (**c**) SAED patterns of $BiVO_4$.

patterns of the pristine MIL-125 as well as in the composite materials and none have been reported in literature which could mean it is not an SAED active material. Morphologies of the MIL-125(Ti) and $BiVO_4$ were not distorted by the formation of the heterojunctions.

Crystallographic studies were further elucidated on XRD illustrated in Fig. 4A and they confirmed monoclinic phases for platelet-like $BiVO_4$ shown by (**a**). Monoclinic $BiVO_4$ was also observed in the composite materials in (**b**-**d**) for 1–1, 3-2 and 2–3 Bi:Ti respectively. These results confirmed what was seen on the SAED patterns. These were indexed to the ICDD card 04-016-4328. Characteristic XRD patterns of MIL-125(Ti) were displayed in (e) which are consistent with literature[26,28–30]. This signaled that the MIL-125 Ti based MOF was successfully synthesized. An appearance of MIL-125(Ti) peaks were observed in all the fabricated composites as shown by the expanded regions in Fig. 1(a,c). The crystallinity of $BiVO_4$ is much defined than that of MIL-125(Ti) which might

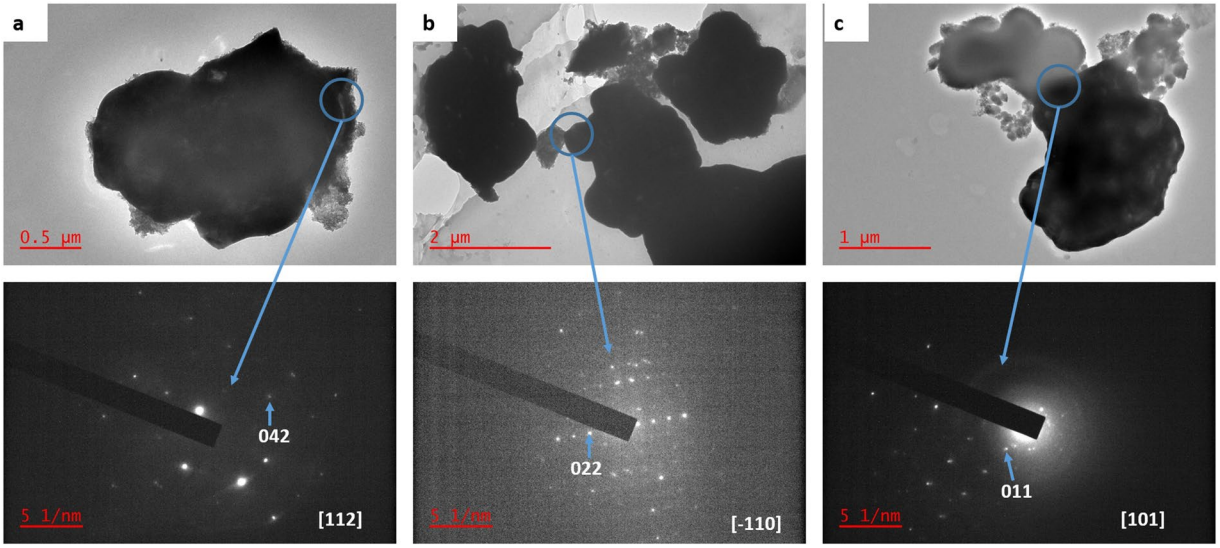


**Figure 3.** TEM images and respective SAED patterns of (**a**) 1–1 Bi:Ti, (**b**) 2–3 Bi:Ti and (**c**) 3-2 Bi:Ti composites of MIL-125(Ti)/$BiVO_4$.

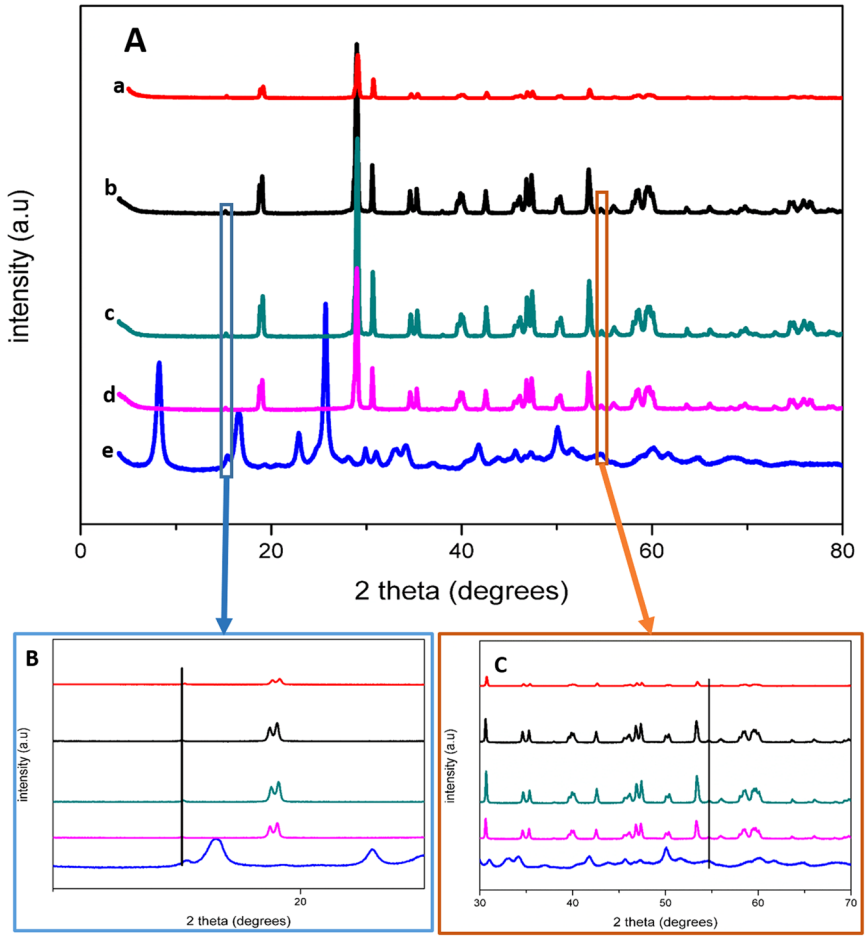


**Figure 4.** (**A**) XRD patterns of (a) $BiVO_4$, (b) 1–1 Bi:Ti, (c) 3–2 Bi:Ti, (d) 2–3 Bi:Ti and (e) MIL-125(Ti). (**B**,**C**) are zoomed in images showing MIL-125(Ti) patterns in the composites.

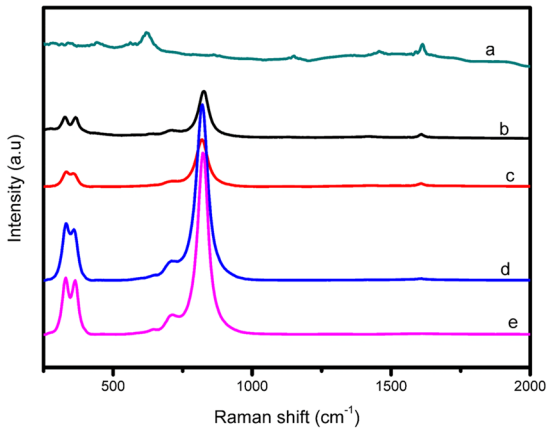


**Figure 5.** Raman spectra of (**a**) MIL-125(Ti), (**b**) 1–1 Bi:Ti (**c**) 2–3 Bi:Ti, (**d**) 3-2 Bi:Ti and (**e**) $BiVO_4$.

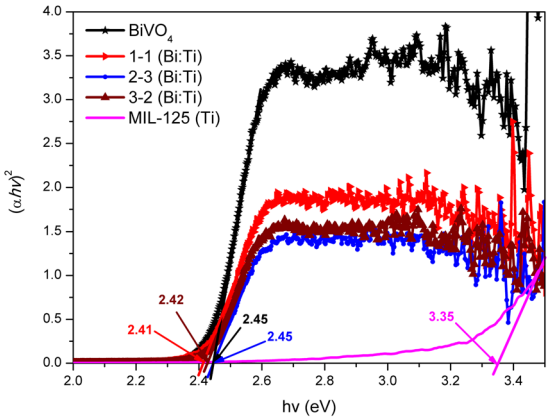


**Figure 6.** Tauc plots of the synthesized nanoparticles.

be causing the $BiVO_4$ patterns to be superior to those of MIL-125. This is similar to the work reported by Yang *et al.*, $BiVO_4$/MIL-125 showed a gradual weakening of MIL-125(Ti) patterns while patterns ascribed to $BiVO_4$ were intensified, which suggested the dominance of $BiVO_4$ in the composites[26]. This was a further affirmation of the successful hybridization of MIL-125(Ti) and $BiVO_4$ composites and confirmed by SEM and TEM imagery.

Further investigation of the crystal phases was conducted by Raman spectroscopy (Fig. 5). The bands indexed at 634, 864, 1145, 1431, 1447 and 1617 $cm^{-1}$ are characteristic of pristine MIL-125(Ti) in Fig. 5(a) and similar Raman bands were reported by Yuan and co-workers[22]. The bands are due to the vibration modes of the organic constituent $H_2BDC$ of this titanium based MOF[31,32]. Conclusively these bands correspond to the asymmetric and symmetric vibrational modes of the carboxylate group in addition to the vibrational modes of the C–H and C=C bonds of the benzene ring[22]. The variations of the Raman bands further confirmed the successful fabrication of MIL-125(Ti). Raman bands re-affirmed the monoclinic phase of platelet-like $BiVO_4$ which complimented the XRD and SAED findings. Bands centred at 209, 323, 370, 708, and 830 $cm^{-1}$ are representative of $BiVO_4$[33]. Raman bands appearing at 830 and 708 $cm^{-1}$ are ascribed to symmetric and asymmetric V–O stretching modes respectively. Those at 370 and 323 $cm^{-1}$ are symmetric and asymmetric bending vibration of $VO_4^{3-}$ tetrahedra respectively[33]. In the composite materials (Fig. 5(b–d)), the bands of both MIL-125(Ti) and monoclinic $BiVO_4$ were observed. The band of MIL-125(Ti) at 1617 $cm^{-1}$ was consistent in all the composites however it weakened with increasing amounts of $BiVO_4$. The appearance of bands at 209, 323 and 830 $cm^{-1}$ are indicative of monoclinic $BiVO_4$ and were also consistent in all the composite materials. The presence of the mentioned bands of both MIL-125(Ti) and monoclinic $BiVO_4$ confirmed the successful fabrication of the heterojunctions. Thus, the formation of the heterojunctions was concretely proved by SEM, TEM, XRD and Raman.

The optical properties of the NPs are shown in Fig. 6 and Figure S6. The band gap of the synthesized NPs, as indirect semiconductors, were calculated using Equation (1) using the DRS data[34].

$$\alpha h\nu = A(h\nu - E_g)^{n/2} \quad (1)$$

where $\alpha$ is the absorption coefficient, $h$ is Plank's constant, $\nu$ is the incident light frequency, A is a constant, $E_g$ is the band gap energy and $n$ is 2. The computed band gaps from $h\nu(eV) = \frac{1240}{\lambda}$ on the $(\alpha h\nu)^2$ versus $h\nu$ plots are shown in Fig. 6. A red shift of the band gaps was observed for the heterojunctions which is caused by the

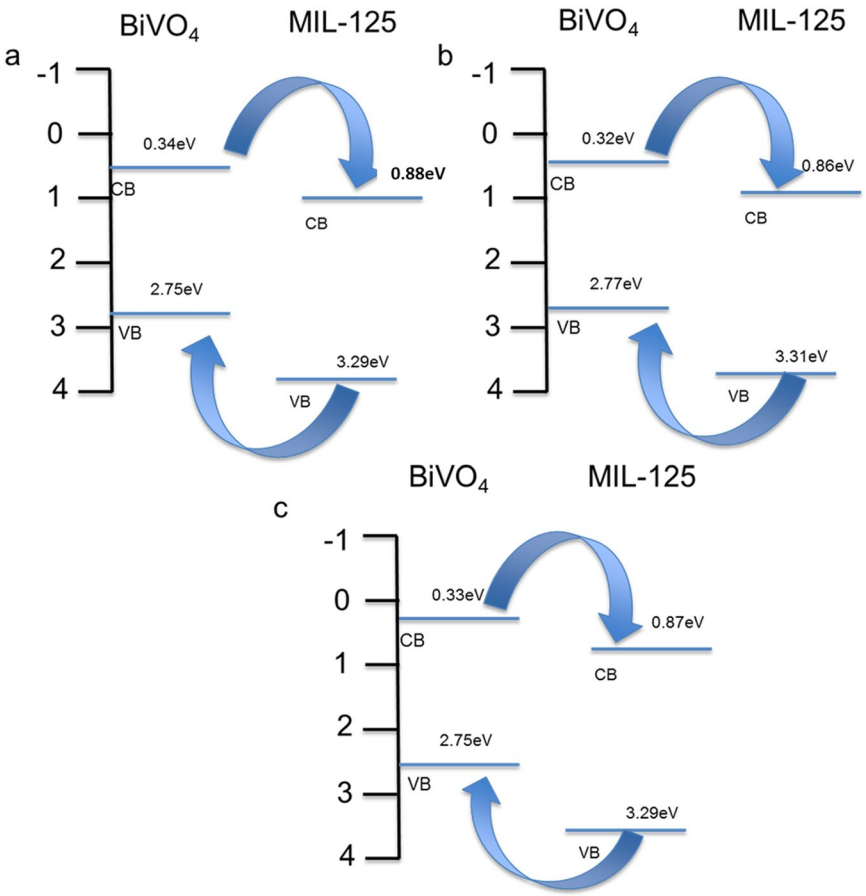


**Figure 7.** Band positions of the heterojunctions (**a**) 1–1 Bi:Ti, (**b**) 2–3 Bi:Ti and (**c**) 3-2 Bi:Ti.

formation of the heterojunctions. It was also affirmed that platelet-like $BiVO_4$ absorbs in the visible region[35], while MIL-125(Ti) is UV active[26]. The band gaps of the pristine and composite materials are shown in Fig. 6.

The energy levels of the material were computed using the following empirical Equations (2 and 3):

$$E_{VB} = X - E^0 + 0.5E_g \tag{2}$$

$$E_{CB} = E_{VB} - E_g \tag{3}$$

where $E_{VB}$ and $E_{CB}$ are the valence and conduction band (VB and CB) potentials respectively. Additionally $E^0$ is the free electrons energy vs normal hydrogen electrode (*ca*. 4.5 eV) and $X$ is the electronegativity of the semiconductor, expressed as the geometric average of the absolute electronegativity of the atoms[15]. The electronegativity of MIL-125(Ti) was computed to be approximately 6.58 eV, while that of $BiVO_4$ was deduced from literature as 6.04 eV. The respective band positions are illustrated in Fig. 7 and they confirm successful formation of the heterojunctions for all the composites, specifically 1–1, 2–3 and 3-2 Bi:Ti in Fig. 7(a–c) respectively. Positioning of the CBs and VBs in the composites were well suited for the separation of electrons and holes during photoexcitation. This will allow the flow of electron from the platelet-like $BiVO_4$ CB to MIL-125(Ti) CB while the holes would migrate from the MIL-125(Ti) VB to platelet-like $BiVO_4$ VB and this would provide a spatial separation of the electrons and holes, which is propitious for improved photocatalytic activity. Literature reports that MIL-125(Ti) has a photochromic behaviour which is linked to the existence of intervalence electron transfer bands as a result of the optically induced movement of electrons to form $Ti^{3+}$ from $Ti^{4+}$ sites in the Ti oxo-clutters of MIL-125(Ti)[28]. Since MIL-125(Ti) cannot be excited by visible light but $BiVO_4$ can, the visible light excited electrons in the $BiVO_4$ are transferred via the intervalence electron transfer bands to reduce $Ti^{4+}$ to $Ti^{3+}$ in the Ti oxo-cluster in the MIL-125(Ti)[29]. Furthermore, the changes of the MIL-125(Ti) energy levels was perhaps caused by the alignment of the intervalence electron transfer bands to the fermi levels of $BiVO_4$, that are closer to the conduction band, when the Schottky contacts are formed. The intervalence electron transfer mechanisms are shown in Equation (4, 5). The band positions of the pristine MIL-125(Ti) and platelet-like $BiVO_4$ are shown in Figure S7.

$$BiVO_4 + h\nu \rightarrow BiVO_4(e^- + h^+) \tag{4}$$

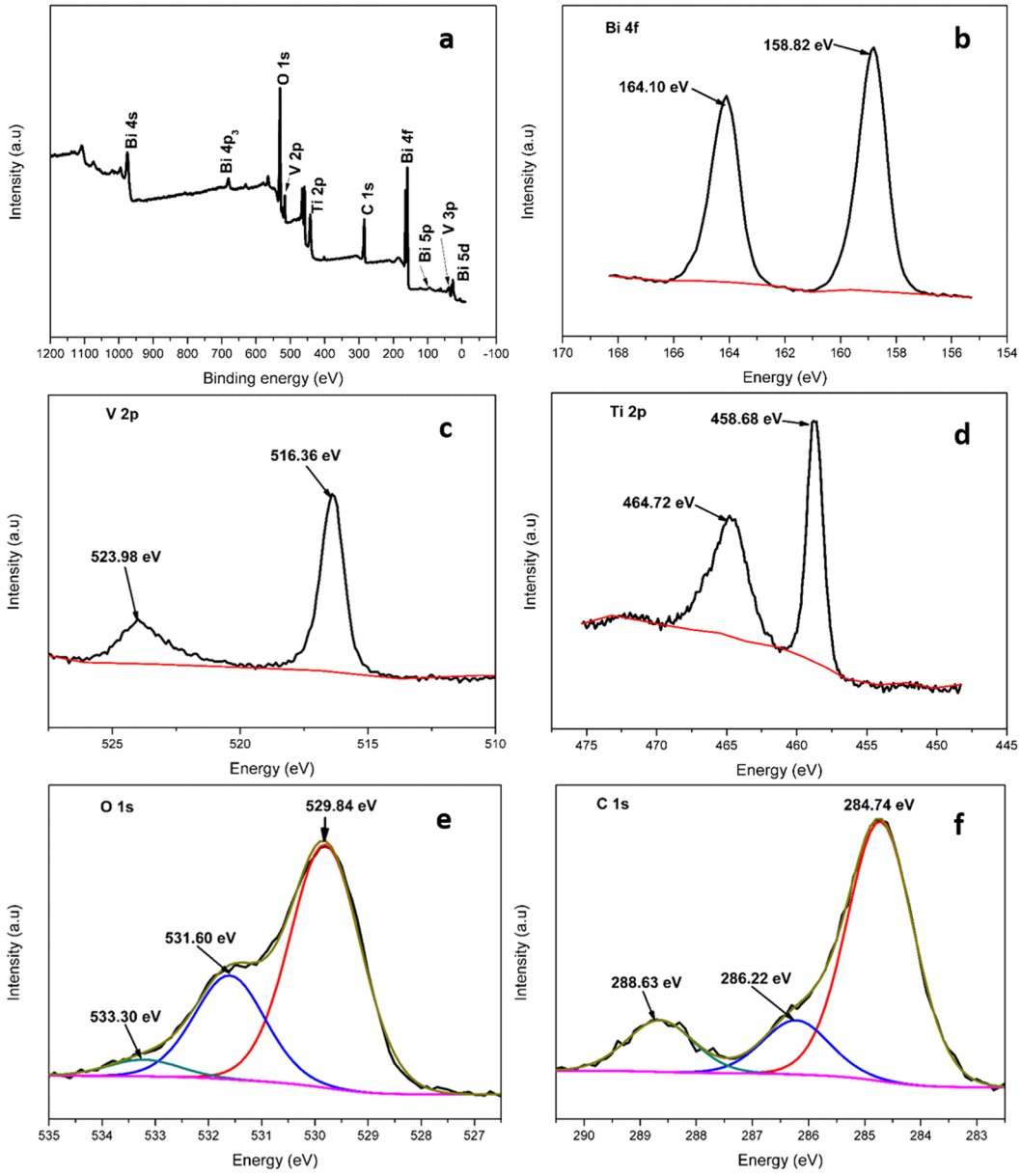


**Figure 8.** The XPS spectra of 3-2 Bi:Ti; (**a**) full survey spectrum, (**b**) Bi 4 f spectrum, (**c**) V 2p spectrum, (**d**) Ti 2p spectrum, (**e**) O 1 s spectra and (**f**) C 1 s spectra.

$$\mathrm{MIL-125(Ti)} + e^{-} \rightarrow \mathrm{Ti^{3+}-MIL-125(Ti)} \quad (5)$$

To ascertain the elemental constitution, chemical state and further confirm the formation of the heterojunction, XPS analysis was carried out. Figures 8a–f (3-2 Bi:Ti) depicts the XPS spectra together with the deconvoluted XPS peaks of Bi, V, Ti, O while the $BiVO_4$ survey spectrum is shown in Figure S8. The survey spectrum depicted in Fig. 8a indicates the presence of O, V, Ti, C and Bi in the 3-2 Bi:Ti composite. The Bi 4 f spectrum in Fig. 8b displays peaks centred at 164.90 eV and 159.60 eV attributable to Bi $4f_{5/2}$ and Bi $4f_{7/2}$.respectively. The difference between the binding energies is 5.28 eV confirming the existence of $Bi^{3+}$ in the composite[36]. The regional spectrum of V in Fig. 8c presents two peaks at 517.20 eV and 524.10 eV attributed to V $2p_{3/2}$ and V $2p_{1/2}$ which indicates that vanadium in the composite exists in +5 oxidation state[37]. Figure 8d depicts the Ti 2p spectra of Bi-Ti. The binding energy values of Ti $2p_{3/2}$ and Ti $2p_{1/2}$ at 458.80 and 465.90 eV correspondingly indicating that titanium bounded to oxygen exists as $Ti^{4+}$ for titanium -oxo-cluster[26,29]. The spectrum of O1s is presented in Fig. 8e and was deconvoluted into three peaks attributed to oxygen from the Ti–O bond in the titanium-oxo-cluster at 529.84 eV, oxygen in hydroxyl groups at 531.60 eV and oxygen atoms in carboxyl groups at 533.30 eV[22]. Figure 8f displays the spectra of C1s which was resolved into three peaks ascribed to C–O at 284.74 eV and 286.22 eV, and

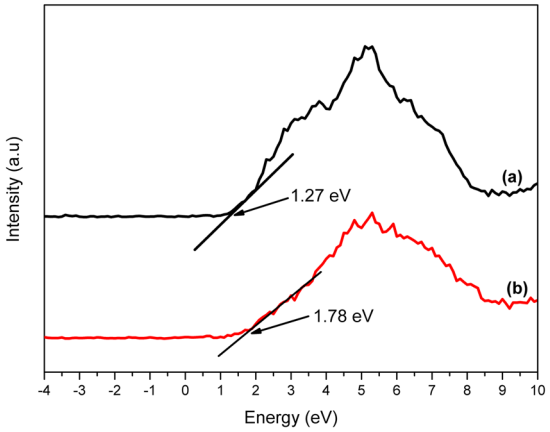


**Figure 9.** The VBs spectra of (**a**) $BiVO_4$ and (**b**) 3-2 Bi:Ti.

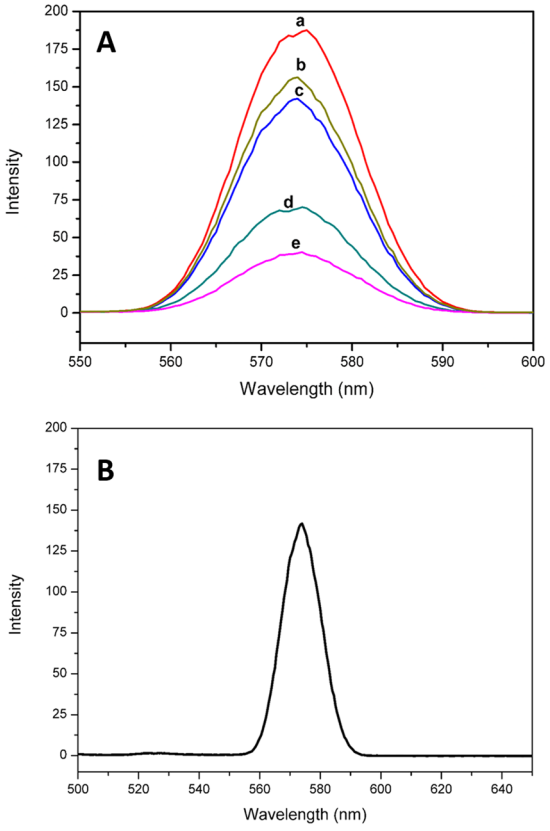


**Figure 10.** (**A**) PL measurements of (a) platelet-like BiVO4, (b) 3-2 Bi:Ti (PM), (c) 1–1 Bi:Ti, (d) 2–3 Bi:Ti and (e) 3-2 Bi:Ti. (**B**) PL measurement of MIL-125(Ti).

O–C=O at 288.63 eV. These were attributed to the MIL-125(Ti) framework, which confirmed that MIL-125(Ti) was formed instead of $TiO_2$.

These results conclusively validate the formation of a heterojunction between MIL-125 and $BiVO_4$. Further proof was observed on the XPS VBs data that showed a more positive shift of the 3-2 Bi:Ti (1.78 eV) VB when compared to the $BiVO_4$ VB of 1.27 eV (Fig. 9). The data firmly affirmed that the resulting heterojunction would be more suited for the photodegradation of organics in water or in oxygen production in water-splitting. As observed from the qualitative calculation of the VB potentials using DRS, the heterojunction was expected to show minimum recombination, and this was confirmed by the XPS data which gives more precise numerical values of the valence band edge potential of the materials.

Photoluminescence (PL) spectra of the NPs is depicted on Fig. 10A. Data from the PL yields information about the electronic properties of the NPs, whereby the intensity of the graphs gives an insight about the recombination

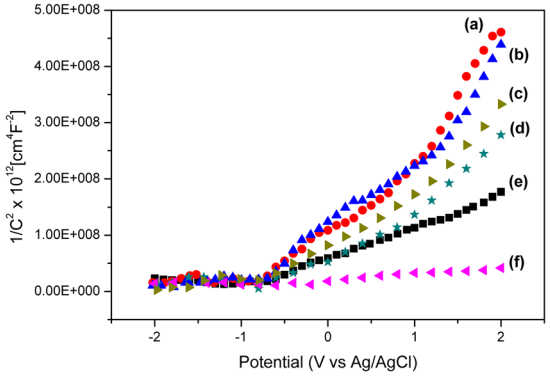


**Figure 11.** Mott-Schottky plots of (**a**) platelet-like $BiVO_4$, (**b**) MIL-125(Ti), (**c**) 3-2 Bi:Ti (PM), (**d**) 1–1 Bi:Ti, (**e**) 2–3 Bi:Ti and (**f**) 3-2 Bi:Ti.

rate of photogenerated charge carriers in the NPs. This is specifically about the availability of surface states and appropriate data about the capability of NPs to trap charges. To correlate PL and mitigation of recombination in photoactive materials, reported in literature is that decreased intensity shows less recombination of photogenerated charge carriers[38]. Thus, there would be inhibited recombination in 3-2 Bi:Ti, followed by 2–3 and 1–1 Bi:Ti shown by Fig. 10A (d), (c) and (b) respectively. The highest recombination was observed for platelet-like $BiVO_4$. The MIL-125(Ti) has an overlapping intensity to that of 1–1 Bi:Ti composite which justifies why it was plotted separately in Fig. 8B. This inferred comparable recombination rates for the materials. Perhaps the quality of the Schottky contact is not favourable enough to effectively facilitate the separation of the electrons and holes in 1–1 Bi-Ti. Furthermore, a physically mixed composite of $BiVO_4$ and MIL-125(Ti) (3-2 Bi:Ti (PM)) was fabricated to investigate the quality of the Schottky contact formed (Fig. 10A). The physically mixed intermediate exhibited a strong peak compared to the heterojunction intermediates indicating that there was no interface formed when the materials were physically mixed as a high recombination rate translates to poor separation efficiency of electrons and holes.

As deduced from the potentiostat, Mott-Schottky plots were plotted through Equation (6) to understand the result of heterostructure formation.

$$\frac{1}{C^2} = \frac{2}{\varepsilon\varepsilon_0 e_0 N_D}\left(E - E_{FB} - \frac{kT}{e_0}\right) \tag{6}$$

where $\varepsilon$ is semiconductor electrode permittivity, $e_0$ is elementary charge, $N_D$ is donor density, $E$ is applied potential, $E_{FB}$ is flat-band potential, $k$ is Boltzmann constant, T is operation temperature and $C$ is capacitance of space charge. The Mott-Schottky plots are shown in Fig. 11 and they presented good correlation to the PL data. The given slope computed from $1/C^2$ against $E$ according to Equation (6) which was further used to observe recombination rates of the NPs. A decreased slope after the formation of the heterojunctions signifies reduced recombination rates of electrons and holes[15]. As observed, the recombination rate was in the following order; platelet-like $BiVO_4$ > MIL-125(Ti) > 1–1 Bi:Ti > 2–3 Bi:Ti > 3-2 Bi:Ti which compared well to the PL data (Fig. 10). The physically mixed (PM) composite (3-2 Bi:Ti (PM)) had a slope lower than that of the pristine materials but higher than that of the composite which further showed that the hydrothermally synthesised heterojunctions successfully formed Schottky contacts that lead to the separation of photoinduced charge carriers. All the NPs slopes that are positive, and this is typical to *n*-type semiconductors. Thus, both platelet-like $BiVO_4$ and MIL-125(Ti) are *n*-type semiconductors.

Electrochemical impedance spectroscopy (EIS) in the form of Nyquits plots was used to investigate the interfacial phenomena that happens between the electrolytes and the photoelectrode. Interpretation of EIS done through the Nyquist plots gives differences in recombination rates by studying the diameters of semicircles formed between real (Z' (Ω)) parts and imaginary (Z"(Ω)) parts of complex impedance. This then translates to a larger semicircle diameter signifying larger charge transfer resistance of the working electrode thus higher recombination rates. The Nyquist plot may in some cases have a semicircle that joins to another larger semicircle or nonvertical line at intermediate frequencies. The second semicircle or nonvertical line gives insights on the electrode roughness. The initial semicircle is ascribed to the charge transfer resistance or electrolyte resistance. The larger semicircle is atributed to limitation of ion transport in the electrolyte for porous electrode structures[39]. Figure 12 then illustrates the synthesized NPs' Nyquist plots. The charge resistance was observed to decrease in the order platelet-like $BiVO_4$ > MIL-125(Ti) > 1–1 Bi:Ti > 2–3 Bi:Ti > 3-2 Bi:Ti which confirmed the information observed from the PL data and Mott-Schottky plots. Thus, the optical and electrochemical characterization data showed a successful formation of *n-n* junctions between platelet-like $BiVO_4$ and MIL-125(Ti) with the optimum being at 3-2 Bi:Ti. This was further proved by the physically mixed composite 3-2 Bi:Ti (PM) which had a high recombination rate compared to the hydrothermally sythesized heterojunctions shown by its larger larger semicircle. This signifies that the formation of hetero-interfaces enhances the separation of photoinduced charge carriers thus inhibiting recombination.

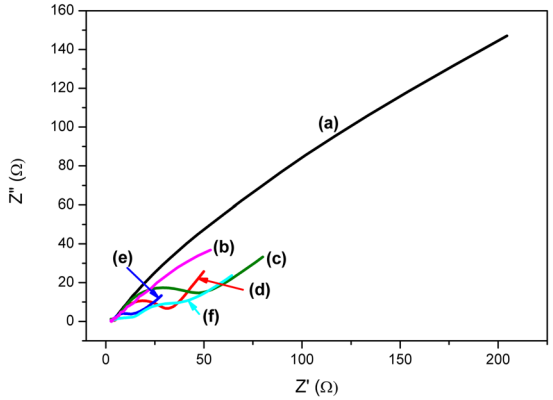


**Figure 12.** Nyquist plots of (**a**) platelet-like $BiVO_4$, (**b**) 3-2 Bi:Ti (PM), (**c**) MIL-125(Ti), (**d**) 1–1 Bi:Ti, (**e**) 2–3 Bi:Ti and (**f**) 3-2 Bi:Ti.

## Conclusion

Different $BiVO_4$-MIL-125(Ti) with diverse molar ratios of Bi:Ti were synthesized through a two-step hydrothermal synthesis protocol. The results revealed that the different heterojunctions were successfully synthesized. Confirmation of the formation of the heterojunction was substantiated by the XPS data which showed a positive shift of the VB in the 3-2 Bi:Ti photocatalyst. The shift also shows that the heterojunction formed would be more suited for the degradation of organics in water as a more positive VB favours the photodegradation of organics in water. Furthermore, the optical and photoelectrochemical studies showed that the photocatalyst 3-2 Bi:Ti exhibited the slowest recombination rate and the fastest interfacial charge shuttle permitted by the *n-n* junction formed. The synthesis of $BiVO_4$-MIL-125(Ti) heterojunction can possibly expand the scope of semiconductor-MOF heterojunctions with expected new properties and applications.

## References


1. Ameta, R., Solanki, M. S., Benjamin, S. & Ameta, S. C. Advanced oxidation processes for wastewater treatment. *Emerg. Green Chem. Tech*; https://doi.org/10.1016/B978-0-12-810499-6.00006-1(2018).
2. Bogdan, J., Jackowska-Tracz, A., Zarzyńska, J. & Pławińska-Czarnak, J. Chances and limitations of nanosized titanium dioxide practical application in view of its physicochemical properties. *Nanoscale Res. Lett.* **10**, 1–10 (2015).
3. Nakata, K. & Fujishima, A. $TiO_2$ photocatalysis: design and applications. *J. Photochem. Photobiol. C Photochem. Rev.* **13**, 169–189 (2012).
4. Amato, C. A. D. *et al*. Band gap implications on nano-$TiO_2$ surface modification with ascorbic acid for visible light-active polypropylene coated photocatalyst. *Nanomaterials* **8**, 599 (2018).
5. Pingmuang, K. *et al*. Composite photocatalysts containing $BiVO_4$ for degradation of cationic dyes. *Sci. Rep.* **7**, 8929 (2017).
6. Wang, R. *et al*. Enhanced visible-light-driven photocatalytic sterilization of tungsten trioxide by surface-engineering oxygen vacancy and carbon matrix. *Chem. Eng. J.* **348**, 292–300 (2018).
7. Wei, Z., Zhao, Y., Fan, F. & Li, C. The property of surface heterojunction performed by crystal facets for photogenerated charge separation. *Comput. Mater. Sci.* **153**, 28–35 (2018).
8. Tang, Z. K. *et al*. Spatial separation of photo-generated electron-hole pairs in BiOBr/BiOI bilayer to facilitate water splitting. *Sci. Rep.* **6**, 1–9 (2016).
9. Tayyebi, A., Soltani, T., Hong, H. & Lee, B. K. Improved photocatalytic and photoelectrochemical performance of monoclinic bismuth vanadate by surface defect states (Bi1-x$VO_4$). *J. Colloid Interface Sci.* **514**, 565–575 (2018).
10. Soltani, T., Tayyebi, A. & Lee, B. K. Enhanced photoelectrochemical (PEC) and photocatalytic properties of visible-light reduced graphene-oxide/bismuth vanadate. *Appl. Surf. Sci.* **448**, 465–473 (2018).
11. Luo, Q., Zhang, L., Chen, X., Tan, O. K. & Leong, K. C. Mechanochemically synthesized m-$BiVO_4$ nanoparticles for visible light photocatalysis. *RSC Adv.* **6**, 15796–15802 (2016).
12. Yang, H. *et al*. New understanding on photocatalytic mechanism of nitrogen-doped graphene quantum dots-decorated $BiVO_4$ nanojunction photocatalysts. *ACS Omega* **2**, 3766–3773 (2017).
13. Joo, E. J. *et al*. Efficient photoelectrochemical water oxidation by metal-doped bismuth vanadate photoanode with iron oxyhydroxide electrocatalyst. *J. Nanomater.* **2016** (2016).
14. Han, J. Y. H., Li, C. & Wang, D. Roles of cocatalysts in photocatalysis and photoelectrocatalysis. *Acc. Chem. Res.* **46**, 1900–1909 (2015).
15. Ye, K.-H. *et al*. Facile synthesis of bismuth oxide/bismuth vanadate heterostructures for efficient photoelectrochemical cells. *RSC Adv.* **5**, 34152–34156 (2015).
16. Wang, R. *et al*. $BiVO_4$/$TiO_2$(N2) Nanotubes heterojunction photoanode for highly efficient photoelectrocatalytic applications. *Nano-Micro Lett.* **9**, 1–9 (2017).
17. Jo, W. J. *et al*. Phase transition-induced band edge engineering of $BiVO_4$ to split pure water under visible light. *Proc. Natl. Acad. Sci.* **112**, 13774–13778 (2015).
18. Tan, H. L., Wen, X., Amal, R. & Ng, Y. H. $BiVO_4${010} and {110} Relative exposure extent: governing factor of surface charge population and photocatalytic activity. *J. Phys. Chem. Lett.* **7**, 1400–1405 (2016).
19. Huang, Z., Pan, L., Zou, J., Zhang, X. & Wang, L. Nanostructured bismuth vanadate-based materials for solar-energy-driven, https://doi.org/10.1039/C4NR05245E (2014).
20. Haag, R. Dendrimers and hyperbranched polymers as high-loading supports for organic synthesis. *Chemistry - A European Journal* **7**, 327–335 (2001).
21. Mathumba, P., Kuvarega, A. T., Dlamini, L. N. & Malinga, S. P. Synthesis and characterisation of titanium dioxide nanoparticles prepared within hyperbranched polyethylenimine polymer template using a modified sol–gel method. *Mater. Lett.* **195**, 172–177 (2017).

22. Yuan, X., Wang, H., Wu, Y. & Zeng, G. One-pot self-assembly and photoreduction synthesis of silver nanoparticle-decorated reduced graphene oxide/MIL-125 (Ti) photocatalyst with improved visible light photocatalytic activity **2016** (2016).
23. Lee, Y., Kim, J. & Ahn, W. Synthesis of metal-organic frameworks: a mini review. *Korean J. Chem. Eng.* **30**, 1667–1680 (2013).
24. Dhakshinamoorthy, A., Asiri, A. M. & García, H. Metal-Organic Framework (MOF) compounds: photocatalysts for redox reactions and solar fuel production. *Angew. Chemie - Int. Ed.* **55**, 5414–5445 (2016).
25. Zhu, J., Li, P. Z., Guo, W., Zhao, Y. & Zou, R. Titanium-based metal–organic frameworks for photocatalytic applications. *Coord. Chem. Rev.* **359**, 80–101 (2018).
26. Yang, Z. *et al*. Preparation of $BiVO_4$/MIL-125(Ti) composite with enhanced visible-light photocatalytic activity for dye degradation. *Appl. Organomet. Chem.* **32**, 1–10 (2018).
27. Mahlalela, L. C. *et al*. Synthesis of platelet-like BiVO4 using hyperbranched polyethyleneimine for the formation of heterojunctions with Bi2O3. *Appl. Nanosci*, https://doi.org/10.1007/s13204-019-00977-8 (2019).
28. Dan-hardi, M. & Serre, C. A new photoactive crystalline highly porous titanium(IV) dicarboxylate. *J. American Chem. Soc*. 10857–10859 (2009).
29. Wang, H. *et al*. Facile synthesis of amino-functionalized titanium metal-organic frameworks and their superior visible-light photocatalytic activity for Cr(VI) reduction. *J. Hazard. Mater.* **286**, 187–194 (2015).
30. Wang, H. *et al*. Applied Catalysis B: Environmental Synthesis and applications of novel graphitic carbon nitride/ metal-organic frameworks mesoporous photocatalyst for dyes removal. *Applied Catal. B, Environ.* **174–175**, 445–454 (2015).
31. Petit, C. & Bandosz, T. J. Synthesis, characterization, and ammonia adsorption properties of mesoporous metal-organic framework (MIL(Fe))-graphite oxide composites: Exploring the limits of materials fabrication. *Adv. Funct. Mater.* **21**, 2108–2117 (2011).
32. Zhang, Y., Li, G., Lu, H., Lv, Q. & Sun, Z. Synthesis, characterization and photocatalytic properties of MIL-53(Fe)-graphene hybrid materials. *RSC Adv.* **4**, 7594–7600 (2014).
33. Zhao, Y., Li, R., Mu, L. & Li, C. Significance of crystal morphology controlling in semiconductor-based photocatalysis: a case study on $BiVO_4$ photocatalyst. *Cryst. Growth Des.* **17**, 2923–2928 (2017).
34. Tumuluri, A., Naidu, K. L. & Raju, K. C. J. Band gap determination using Tauc's plot for LiNbO3 thin films. *Int. J. ChemTech Res* **6**, 3353–3356 (2014).
35. Ye, K. *et al*. RSC Advances Facile synthesis of bismuth oxide/bismuth vanadate heterostructures for efficient. *RSC Adv.* **5**, 34152–34156 (2015).
36. Zhang, A. & Zhang, J. Synthesis and characterization of Ag/$BiVO_4$ composite photocatalyst. *Appl. Surf. Sci.* **256**, 3224–3227 (2010).
37. Li, H. *et al*. Hydrothermal Synthesis of Novel $MoS_2$/$BiVO_4$ Hetero-nanoflowers with enhanced photocatalytic activity and a mechanism investigation. *J. Phys. Chem. C* **119**, 22681–22689 (2015).
38. Das, S. N., Kar, J. P., Choi, J., Byeon, S. & Jho, Y. D. Influence of surface morphology on the optical property of vertically aligned ZnO nanorods. *Appl. Phys. Lett.* **95**, 1–4 (2015).
39. Mei, B. A., Munteshari, O., Lau, J., Dunn, B. & Pilon, L. Physical interpretations of nyquist plots for EDLC electrodes and devices. *J. Phys. Chem. C* **122**, 194–206 (2018).


## Acknowledgements

The authors would like to pass their sincere thanks to the following funders of the work; The authors would like to acknowledge the University of Johannesburg (URC) and Faculty of Science (FRC), Centre for Nanomaterials Science Research and Eskom (TESP) for financial support.

## Author Contributions

P.V. Hlophe and L.C. Mahlalela were responsible for synthesis and characterization of materials. They further analysed the results and wrote the manuscript text. L.N. Dlamini was responsible for the supervision of the work, structuring and review of the manuscript.

## Additional Information

**Supplementary information** accompanies this paper at https://doi.org/10.1038/s41598-019-46498-w.

**Competing Interests:** The authors declare no competing interests.

**Publisher's note:** Springer Nature remains neutral with regard to jurisdictional claims in published maps and institutional affiliations.